Ultrahigh field diffusion magnetic resonance imaging uncovers intriguing microstructural changes in the adult zebrafish brain caused by Toll-like receptor 2 genomic deletion

Singer, R; Oganezova, I.; Hu, W.; Liu, L.; Ding, Y.; Groot, H.J.M.; … ; Alia, A.

RESEARCH ARTICLE

Ultrahigh field diffusion magnetic resonance imaging uncovers intriguing microstructural changes in the adult zebrafish brain caused by Toll-like receptor 2 genomic deletion

Rico Singer[1] | Ina Oganezova[1] | Wanbin Hu[2] | Li Liu[2] | Yi Ding[2] |
Huub J. M. de Groot[1] | Herman P. Spaink[2] | A. Alia[1,3]

[1]Leiden Institute of Chemistry, Leiden University, Leiden, The Netherlands

[2]Institute of Biology, Leiden University, Leiden, The Netherlands

[3]Institute of Medical Physics and Biophysics, Leipzig University, Leipzig, Germany

Correspondence
A. Alia, Leiden Institute of Chemistry, Leiden University, 2300 RA Leiden, The Netherlands.
Email: a.alia@chem.leidenuniv.nl

Abstract

Toll-like receptor 2 (TLR2) belongs to the TLR protein family that plays an important role in the immune and inflammation response system. While TLR2 is predominantly expressed in immune cells, its expression has also been detected in the brain, specifically in microglia and astrocytes. Recent studies indicate that genomic deletion of TLR2 can result in impaired neurobehavioural function. It is currently not clear if the genomic deletion of TLR2 leads to any alterations in the microstructural features of the brain. In the current study, we noninvasively assess microstructural changes in the brain of TLR2-deficient ($tlr2^{-/-}$) zebrafish using state-of-the art magnetic resonance imaging (MRI) methods at ultrahigh magnetic field strength (17.6 T). A significant increase in cortical thickness and an overall trend towards increased brain volumes were observed in young $tlr2^{-/-}$ zebrafish. An elevated T_2 relaxation time and significantly reduced apparent diffusion coefficient (ADC) unveil brain-wide microstructural alterations, potentially indicative of cytotoxic oedema and astrogliosis in the $tlr2^{-/-}$ zebrafish. Multicomponent analysis of the ADC diffusivity signal by the phasor approach shows an increase in the slow ADC component associated with restricted diffusion. Diffusion tensor imaging and diffusion kurtosis imaging analysis revealed diminished diffusivity and enhanced kurtosis in various white matter tracks in $tlr2^{-/-}$ compared with control zebrafish, identifying the microstructural underpinnings associated with compromised white matter integrity and axonal degeneration. Taken together, our findings demonstrate that the genomic deletion of TLR2 results in severe alterations to the microstructural features of the zebrafish brain. This study also highlights the potential of ultrahigh field diffusion MRI techniques in discerning exceptionally fine microstructural details

within the small zebrafish brain, offering potential for investigating microstructural changes in zebrafish models of various brain diseases.

1 | INTRODUCTION

Pattern recognition receptors (PRRs), encoded in the germline DNA, play a crucial role in the animal immune defence as part of the innate immune system.[1] Unlike T cells and B cells, expressing antigen recognition receptors with a high specificity, PRRs initiate immune response by recognising a diverse array of pathogen-associated molecular patterns (PAMPs) found on various microorganisms. PRRs also recognise danger-associated molecular patterns (DAMPs), produced as a consequence of damaged tissue. Among the eight PRR groups,[2] Toll-like receptors (TLRs) stand out as vital components of the innate immune system. Structurally, TLRs consist of three distinct parts[3]: (i) an N-terminal ectodomain on the membrane outside, responsible for recognising and binding to specific PAMPs or DAMPs; (ii) a transmembrane domain spanning the lipid bilayer of the cell membrane, to anchor the receptor in its place; and (iii) a C-terminal to initiate downstream signalling on the intracellular side of the membrane. Within the TLR family, specific TLRs play crucial roles in distinguishing unique PAMPs and DAMPs. Interestingly, the number of TLRs expressed in various vertebrate species varies. For example, humans possess 10 TLRs encoded in their genome, whereas mice and zebrafish have genomes encoding for at least 12 and 20 functional TLRs, respectively.[4,5] Toll-like receptor 2 (TLR2), one such member of the TLR family, plays a particularly important role in the immune and inflammatory response system and has orthologs in humans, mice and zebrafish. TLR2 is expressed on the cell surface of endothelial, epithelial and immune cells, including macrophages, dendritic cells and monocytes,[6] and forms heterodimers with TLR1 or TLR6.[2] The broad recognition spectrum of TLR2 encompasses a wide range of PAMPs and DAMPs ligands.[2] In addition to its crucial role in the immune and inflammatory response system, TLR2 has become a focal point of interest due to its dual function in the infection processes. While TLR2-mediated inflammatory responses are important for effective bacterial clearance, excessive or inappropriate TLR2 signalling can lead to unintended tissue damage, inflammatory disorders or delayed healing.[7,8] In the brain, excessive TLR2 signalling has emerged as potential player in the pathogenesis of neuroinflammatory and neurodegenerative disorders, including in the pathogenesis of Alzheimer's disease, Parkinson's disease, amyotrophic lateral sclerosis and ischaemic strokes.[9] There are rather conflicting reports on the role of TLR2 deficiency in the brain. Some reports suggest that a deficiency of TLR2 may improve neurobehavioural functions and protect against neurodegenerative diseases.[10] On the other hand, other reports have shown that a deficiency of TLR2 itself could induce cognitive disabilities, decreased locomotor activity and increased anxiety and depression.[11,12] In a TLR2-deficient mouse model, aggravated white matter (WM) damage and deteriorated neurobehavioural functions have been observed in the absence of an infection or neurodegenerative-inducing mutations.[11] Thus, the exact role of TLR2 in regulating normal neurological functions and inducing neuroinflammatory processes remains to be established.

In a recent study, we utilised zebrafish (*Danio rerio*) larvae as an in vivo model to investigate the metabolic control functions of TLR2 through transcriptomic and metabolomic approaches.[2] We showed that the deficiency of TLR2 in zebrafish larvae leads to many metabolic changes compared with controls and proposed that, in addition to its function in immunity and inflammatory processes, TLR2 has a function in controlling metabolism in the absence of infection. However, the impact of TLR deficiency on brain structure and function and neuroinflammation in the absence of infection is not clear. A comprehensive, noninvasive system-level study would be necessary to clarify this. Magnetic resonance imaging (MRI) is a well-established, noninvasive technique. MRI provides distinct advantages compared with other microscopic techniques, even those potentially reaching higher resolutions. This includes its capability for whole-organ imaging, including full 3D analysis, while eliminating the necessity for sectioning or chemical staining. Moreover, recent advancements in MRI gradient systems and ultrahigh magnetic field strength provide the ability to achieve very high spatial resolutions.[13] In our earlier studies we developed MRI methods for (in vivo) imaging of zebrafish,[14,15] which we applied to study various models including cystic leukoencephalopathy,[16] Lowe syndrome,[17] in vivo analysis of tumours[18] and microstructural changes in the muscle tissue of leptin-deficient zebrafish.[19] In vivo MRI also enabled longitudinal studies of live adult zebrafish brain, as reported by Hamilton et al.[20] However, gaining access to microstructural details in the tiny zebrafish brain is challenging. MRI at ultrahigh field in conjunction with mathematical modelling can probe microstructural changes in the tiny zebrafish brain. In addition, diffusion-based MRI (dMRI) offers a remarkable sensitivity to water movement, encompassing techniques including diffusion-weighted imaging (DWI), diffusion tensor imaging (DTI) and diffusion kurtosis imaging (DKI). These techniques provide unique ways for exploring microstructural alterations in the brain and offer noninvasive opportunities to monitor the progression of neurodegenerative disorders.[21,22] Furthermore, dMRI tractography enables the visualisation of WM structures within the zebrafish brain, thereby enabling the precise examination of these anatomical structures.[23]

To elucidate the precise involvement of TLR2 in regulating normal neurological functions and neuroinflammatory processes, we employed TLR2 knockout (KO) (*tlr2*$^{-/-}$) zebrafish as a model organism. By utilising state-of-the-art MRI methods at ultrahigh magnetic field (17.6 T), we explored the

impact of TLR2 deficiency on the microarchitecture of the brain. Ultrahigh field micro-MRI with strong field gradients provides the necessary resolution and signal-to-noise ratio (SNR) required to study the microstructural changes in the tiny zebrafish brain. Furthermore, diffusion-weighted MRI provided superior anatomical and substructural details of the zebrafish brain compared with traditional anatomical imaging. DTI tractography by short-track track-density imaging (stTDI) enabled us to see changes in specific WM structures in TLR2 KO ($tlr2^{-/-}$) zebrafish compared with controls. Our results show that TLR2 deficiency leads to microstructural changes associated with compromised WM integrity and axonal degeneration.

2 | METHODS

2.1 | Zebrafish husbandry

In this study, the wild-type AB/TL strain and $tlr2^{sa19423}$ zebrafish line, obtained from the Sanger Institute Zebrafish Mutation Resource (Hinxton, Cambridge, UK), were utilised. The homozygote carriers of the TLR2 mutation, along with their wild-type control, were subjected to more than five rounds of outcrossing, resulting in the $tlr2^{-/-}$ (mutant) and $tlr2^{+/+}$ (control) siblings used for the experiments described in this work. Screening and raising of $tlr2^{-/-}$ and control zebrafish were performed as previously described,[24,25] complying with university animal welfare committee guidelines (license numbers: AVD1060020171767 and AVD10600202216175), following EU Animal Protection Directive international guidelines (2010/63/EU) and according to standard protocols (www.zfin.org). For imaging, five male pairs of 3-month-old (84 days) $tlr2^{-/-}$ and control zebrafish were euthanised through immobilisation by submersion in ice water (0–4°C) for approximately 10 min, followed by cessation of opercular movement. Specimens were then fixed in 4% buffered paraformaldehyde (Zinc Formal-Fixx, ThermoShandon, UK) for 4 days.

2.2 | Magnetic resonance imaging

MRI experiments were conducted using a Bruker vertical bore system (Bruker Biospin GmbH, Germany) operating at 17.6 T (750 MHz). The system was equipped with a water-cooled MICRO5 gradient system, offering a gradient strength of up to 3 T/m. Additionally, a birdcage transmit and receive radiofrequency (RF) coil with a 5-mm inner diameter and a GREAT60 gradient power supply were employed. Data acquisition and processing were performed with a Linux workstation, running ParaVision 360 v3.3 imaging software (Bruker BioSpin GmbH, Germany). For all experiments, zebrafish were transferred to 5-mm NMR tubes and embedded in perfluoropolyether (Fomblin Y, Solvay Solexis S.P.A.) to remove background signals, while having a susceptibility close to tissue.[26] Maximum signal intensity and magnetic field homogeneity were achieved by aligning the zebrafish brain to the centre of the RF coil and automatic shimming up to the second order. Prior to each experiment, the frequency calibration was fine-tuned, and the reference power and receiver gain were optimised.

For the estimation of T_2, we utilised a multislice multiecho (MSME) pulse sequence, based on the Carr–Purcell–Meiboom–Gill (CPMG) sequence.[27] MSME measurements were performed with 60 echoes per excitation, with a CPMG refocusing pulse interval of $\tau = 6.0$ ms, a repetition time (TR) of 3000 ms and taking $ns = 4$ as the number of scans for data averaging. The field of view (FOV) was 6×6 mm, with a matrix size of 128×128, resulting in an in-plane resolution of 47×47 μm, at a slice thickness of 500 μm and a total scan time of $\sim$25 min.

In a dMRI experiment, a 90° excitation RF pulse is succeeded by a 180° refocusing RF pulse. Manifestation of diffusion dependency is achieved through the application of gradient pulses both before and after the refocusing RF pulse, as originally developed by Stejskal and Tanner.[28] The strength (G), gradient pulse interval (Δ) and gradient pulse length (δ) of these gradient pulses are summarised in the b-value according to $b = \gamma^2 G^2 \delta^2 (\Delta - \frac{\delta}{3})$, where γ is the gyromagnetic ratio. DWI experiments were performed with a diffusion-weighted spin-echo sequence, applying an echo time (TE) of 13.0 ms, $TR = 1000$ ms, $ns = 4$, $\delta = 1$ ms, $\Delta = 7$ ms and an effective b-value range of 50, 500, 1000, 1500, 2000, 2500 or 3000 s/mm^2. The FOV was 6×6 mm, with a matrix size of 128×128, resulting in an in-plane resolution of 47×47 μm, at a slice thickness of 200 μm and a total scan time of $\sim$48 min. DTI utilising echo-planar imaging (EPI) was employed for anatomical imaging of the zebrafish brain. Additionally, this technique enabled the estimation of various diffusion metrics, including axial diffusivity ($D_{\parallel}$), radial diffusivity ($D_{\perp}$), mean diffusivity (MD) and fractional anisotropy (FA), as well as axial kurtosis ($K_{\parallel}$), radial kurtosis ($K_{\perp}$), mean kurtosis tensor (MK) and kurtosis fractional anisotropy (KFA). In addition, DTI-facilitated tractography was used to explore the connectivity of neural pathways within the zebrafish brain. 2D DTI experiments were performed with $TE = 12.4$ ms, $TR = 2000$ ms, $ns = 32$ and an EPI factor of 8. Multishell DTI experiments were performed with $\delta = 1.5$ ms, $\Delta = 6$ ms and an effective b-value range of 4, 1000, 3500 or 6000 s/mm^2, with 8, 12, 24 or 36 directions, respectively. The FOV was 5×5 mm, with a matrix size of 200×200, resulting in an in-plane resolution of 25×25 μm, at a slice thickness of 200 μm and a total scan time of 11 h 22 min. 3D DTI experiments were performed with $TE = 9.1$ ms, $TR = 2000$ ms, $ns = 4$ and an EPI factor of 8. Multishell diffusion experiments were performed with $\delta = 1.5$ ms, $\Delta = 4$ ms and an effective b-value range of 100, 1000 or 2500 s/mm^2, with 4, 12 or 24 directions, respectively. The FOV was $2.52 \times 4.97 \times 1.82$ mm, with a matrix size of $72 \times 142 \times 52$, resulting in an isotropic resolution of 35 μm and a total scan time of 36 h 58 min.

2.3 | Data processing

2.3.1 | Brain structure identification

Identification of brain regions and WM structures was based on various available zebrafish brain atlases and similar sources.[29–31] The cortical thickness of the longitudinal torus (TL), the molecular layer of the cerebellar corpus (CCem) and the optic tectum (TeO) were estimated using the distance-measuring tools in Paravision software (Bruker BioSpin GmbH, Germany). The estimation was based on the central sagittal or coronal slice at a b-value of 2500 s/mm^2 from 3D DTI measurements obtained at 17.6 T. The volume of the main brain regions, including the total brain volume, was estimated using MATLAB R2021b (mathworks.com). Raw DTI data were imported into MATLAB using a modified version of read_2dseq.[32] The mean intensity of the largest acquired b-value was calculated, as it provided the optimal contrast for segmenting the brain into its main regions. The segmentation of brain regions was performed in the Volume Segmenter tool of MATLAB, after which their volumes were calculated based on the applied resolution.

2.3.2 | Estimation of T_2

The estimation of T_2 was performed using MSME data. Uneven echoes were excluded from the data fitting to compensate for imperfect refocusing pulses,[33] and the first 12 remaining echoes (12–144 ms) were used for fitting. After 144 ms, the SNR fell below the threshold value for a Gaussian distribution of the T_2 signal (see Figure S1) required for reliable line-fitting. T_2 was estimated with a nonlinear least square algorithm for the exponential fit function according to

$$I_t = A + I_0 \cdot \exp\left(-t/T_2\right), \tag{1}$$

where I_t is the signal intensity at time t, A is the absolute bias, I_0 is the signal intensity at time t_0 and t is the echo time (ms).

2.3.3 | Estimation of the apparent diffusion coefficient

The estimation of the apparent diffusion coefficient (ADC) was performed from DWI data, with a nonlinear least square algorithm for the exponential fit function:

$$I_b = A + I_0 \cdot \exp\left(-b \cdot ADC\right). \tag{2}$$

Here, I_b is the signal intensity at b, A is the absolute bias and I_0 is the signal intensity at time b_0.

2.3.4 | ADC multicomponent analysis by the phasor approach

Monocomponent and multicomponent ADC analysis by the phasor approach was performed using MATLAB. Raw DWI data were imported into MATLAB. DWI data are transformed to phasor plot coordinates by selecting the region of interest (ROI) using the volume segmenter tool. Next, for each individual ADC decay curve in the ROI, a stepwise approach was followed: (i) an absolute bias systematic error correction was performed, based on a Rayleigh probability distribution fit of the background signal (see Figure S2), then (ii) the data were filtered by an arithmetic mean filter with filter size 2, followed by (iii) normalization to the [0, 1] range, (iv) fast-Fourier transformation, (v) selection of the first harmonics, and, finally (vi) plotting the real versus the imaginary part. The semicircle of the phasor plot, representing the phasor coordinates of monocomponent ADC, is added for ADC between 0 and 0.001 mm^2/s based on Equation (2). Monocomponent analysis of DWI is performed by projecting the phasor plot coordinates of the ROIs onto the semicircle using the MATLAB dsearchn() function. In addition, a bi-component analysis was performed, based on the bi-exponential fit function:

$$I_b = a \cdot \exp\left(-b \cdot ADC_{slow}\right) + c \cdot \exp\left(-b \cdot ADC_{fast}\right). \tag{3}$$

Here, I_b is the signal intensity at b, and a and c are the areas of component ADC_{slow} and ADC_{fast} (s/mm^2), respectively. For this, ADC_{slow} was taken between 0 and $4 \cdot 10^{-4}$ mm^2/s, ADC_{fast} between $4.1 \cdot 10^{-4}$ and $1 \cdot 10^{-3}$ mm^2/s, with a step-size of $1 \cdot 10^{-5}$ mm^2/s, for step-sizes of 1% for a and c. Obtained values were verified by determining the fit (R^2) using the curve fitting tool in MATLAB.

2.3.5 | Processing of DTI data

DTI data processing, including diffusion metrics estimation and WM connectivity analysis by tractography, was conducted using MRtrix3 software[34] and MATLAB. Brain masks were generated using the Volume Segmenter tool in MATLAB. Raw DTI data were denoised based on the random matrix theory and potential Gibbs ringing artifacts were removed based on the method of local subvoxel shifts,[35] implemented through MRtrix3 functionality.[36] The estimations of the (apparent) diffusion tensors ($\mathbf{D}$) and (apparent) diffusion kurtosis tensors ($\mathbf{W}$) were also executed through functionalities available within MRtrix3. $\mathbf{D}$ and $\mathbf{W}$ were derived from logarithmically transformed and preprocessed DTI data through a two-stage procedure. First, the fitting process employed a weighted least-squares methodology, which was based on empirical signal intensities. Second, an iterated weighted least-squares approach was used, utilising the signal predictions from the preceding iteration to inform subsequent iterations. In total, two iterations are performed. Due to their full symmetry, $\mathbf{D}$ and $\mathbf{W}$ have 6 and 15 degrees of freedom, respectively. Construction of $\mathbf{W}$ requires a minimum of 22 diffusion-weighted images taken at three distinct b-values towards 15 unique directions.[37] Full descriptions of the methodology are provided by Basser et al. for $\mathbf{D}$, and by Veraart et al. for $\mathbf{W}$.[38,39] Diffusion tensor metrics ($D_\parallel$, $D_\perp$, MD and FA) were estimated from $\mathbf{D}$, according to

$$D_\parallel = \lambda_1 \tag{4}$$

$$D_\perp = \frac{\lambda_2 + \lambda_3}{2} \tag{5}$$

$$MD = \frac{\lambda_1 + \lambda_2 + \lambda_3}{3}, \text{and} \tag{6}$$

$$FA = \frac{\left\| \mathbf{D} - MD \cdot \mathbf{I}^{(2)} \right\|}{\|\mathbf{D}\|} = \sqrt{\frac{3}{2} \frac{(\lambda_1 - MD)^2 + (\lambda_2 - MD)^2 + (\lambda_3 - MD)^2}{\lambda_1^2 + \lambda_2^2 + \lambda_3^2}}. \tag{7}$$

The λ_1, λ_2 and λ_3 are the eigenvalues of $\mathbf{D}$, arranged such that $\lambda_1 \geq \lambda_2 \geq \lambda_3$, $\mathbf{I}^{(2)}$ is the fully symmetric rank 2 isotropic tensor, and $\|...\|$ denote the application of the Frobenius norm. For the estimation of the diffusion kurtosis tensor metrics, $\mathbf{W}$ was utilised.[40,41] Estimation of MK was based on the equation for rapid MK estimation, as defined by Hansen and Jespersen,[42]

$$MK = \tfrac{1}{5} Tr(\mathbf{W}) \tag{8.1}$$

$$MK = \tfrac{1}{5}(W_{1111} + W_{2222} + W_{3333} + 2W_{1122} + 2W_{1133} + 2W_{2233}), \tag{8.2}$$

where W_{ijkl} are the diffusion kurtosis tensor elements. Estimation of $K_\parallel$ was based on

$$K_\parallel = \frac{(\lambda_1 + \lambda_2 + \lambda_3)}{9\lambda_1^2} W_{1111}. \tag{9}$$

Estimation of $K_\perp$ was based on

$$K_\perp = G_1 W_{2222} + G_1 W_{3333} + G_2 W_{2233}, \tag{10}$$

with

$$G_1 = \frac{(\lambda_1 + \lambda_2 + \lambda_3)^2}{18\lambda_2(\lambda_2 + \lambda_3)^2} \left(2\lambda_2 + \frac{\lambda_3^2 - 3\lambda_2\lambda_3}{\sqrt{\lambda_2\lambda_3}} \right) \text{and} \tag{11}$$

$$G_2 = \frac{(\lambda_1 + \lambda_2 + \lambda_3)^2}{3(\lambda_2 - \lambda_3)^2} \left(\frac{\lambda_2 + \lambda_3}{\sqrt{\lambda_2\lambda_3}} - 2 \right). \tag{12}$$

The estimation of KFA was based on

$$KFA = \frac{\left\| \mathbf{W} - MK \cdot \mathbf{I}^{(4)} \right\|}{\|\mathbf{W}\|}, \tag{13}$$

where $I^{(4)}$ is the fully symmetric rank 4 isotropic tensor and **W** was formed by permutating its 15 unique elements, which were acquired from MRtrix3 software.

2.3.6 | White matter structure identification by DTI tractography

To identify WM structures in the zebrafish brain, tractography was employed using super-resolution (5 μm) stTDI by multishell multitissue constraint spherical deconvolution (stTDI msmt CSD), conducted using the MRtrix3 software.[34] Estimation of the msmt CSD response functions was performed by the Dhollander algorithm,[43] selecting the top 10.0%, 2.0% and 10.0% of refined WM, grey matter (GM) and cerebrospinal fluid (CSF) voxels, respectively. Crude segmentation of WM from GM and CSF was performed at FA 0.15. Fibre orientation distribution functions (fODFs) were estimated using the msmt-CSD algorithm.[44] Whole-brain short-track tractography was performed with the iFOD1 algorithm,[45] generating 10 million tracks, with a length of between two and 10 voxels. The generated tracks were converted to super resolution TDI,[46] obtaining connectivity images at an approximate 5-μm resolution, in which the orientation of tracks is indicated by directional encoded colour (DEC).

2.3.7 | Statistical analysis

All statistical analysis of data was performed using MATLAB and GraphPad Prism version 9.0.0 for Windows (Graphpad Software, San Diego, CA, USA; www.graphpad.com). Test of significance was performed using the unpaired *t*-test, assuming Gaussian distribution, with a *p* value of less than 0.05 considered as a significant difference between the two groups. Possible outliers were identified and removed based on three scaled median absolute deviations from the median value.

3 | RESULTS AND DISCUSSION

In this study, we probed the effect of genomic deletion of TLR2 on microstructural changes observed in the brain of $tlr2^{-/-}$ adult zebrafish noninvasively, utilising state-of-the-art MRI at an ultrahigh magnetic field strength of 17.6 T.

3.1 | Changes in brain morphology observed in $tlr2^{-/-}$ zebrafish brain

Figure 1 presents high-resolution images of control and $tlr2^{-/-}$ male zebrafish, acquired using 3D DTI at a *b*-value of 2500 s/mm². DTI offered enhanced contrast compared with conventional anatomical imaging techniques, enabling clear separation of tiny zebrafish brain structures. Differences in the cortical thickness of brain structures were observed in the cerebellum (CB) and the mesencephalon (MC) (Figure 1A). In the CB, the thickness of the CCem was found to be significantly enlarged by approximately 38% in $tlr2^{-/-}$ zebrafish compared with the control group (Figure 1C). Similar observations were made in the MC, where the volumes of the TL and TeO were significantly increased by approximately 29% and 27%, respectively. To expand upon pathologically derived differences in brain structure observed in $tlr2^{-/-}$ zebrafish, brain volumes were estimated utilising 3D DTI data. The zebrafish brain was divided into its main regions[29,30]: the olfactory bulb (OB), pallium (Pa), diencephalon (DC), MC, CB and rhombencephalon (RC) (Figure 1B). In $tlr2^{-/-}$ zebrafish, a significant increase in the volume of the CB and RC was observed ($p < 0.05$, $n = 3$) compared with the control group. Our results demonstrate an increase in the cortical thickness and a trend towards increased brain volume of the $tlr2^{-/-}$ zebrafish compared with the control group, while the differences in body length and weight between 3-month-old $tlr2^{-/-}$ and control zebrafish were negligible (data not shown). Previously, a significant reduction in the cortex thickness, in combination with WM damage and neuronal loss, was reported for TLR2-deficient mice.[11] In addition, $tlr2^{-/-}$ was associated with significantly reduced levels of insulin-like growth factor 1 (IGF-1), which has neuroprotective properties and plays an important role in neuronal viability and the prevention of apoptosis.[47] While neurodegenerative disorders are typically linked to cortical thinning and reduced brain volumes in their advanced stages, it has been observed that cortical thickening and volumetric increase occur in the initial phases as a reaction to underlying pathological processes.[48,49] The observed increase in cortical thickness could be an early indicator of neurodegenerative processes associated with TLR2 deficiency. Furthermore, increased brain volume may be associated with swelling of the brain due to cerebral oedema, that is, the abnormal swelling of brain cells by accumulation of fluid. Previous studies in $tlr2-/-$ mice have shown hypoperfusion in the brain that could indirectly signify cytotoxic oedema.[50] A longitudinal study, outside the scope of the current work, would be required to provide more insight into the development of changes in cortical thickness and brain volume of $tlr2^{-/-}$ zebrafish.
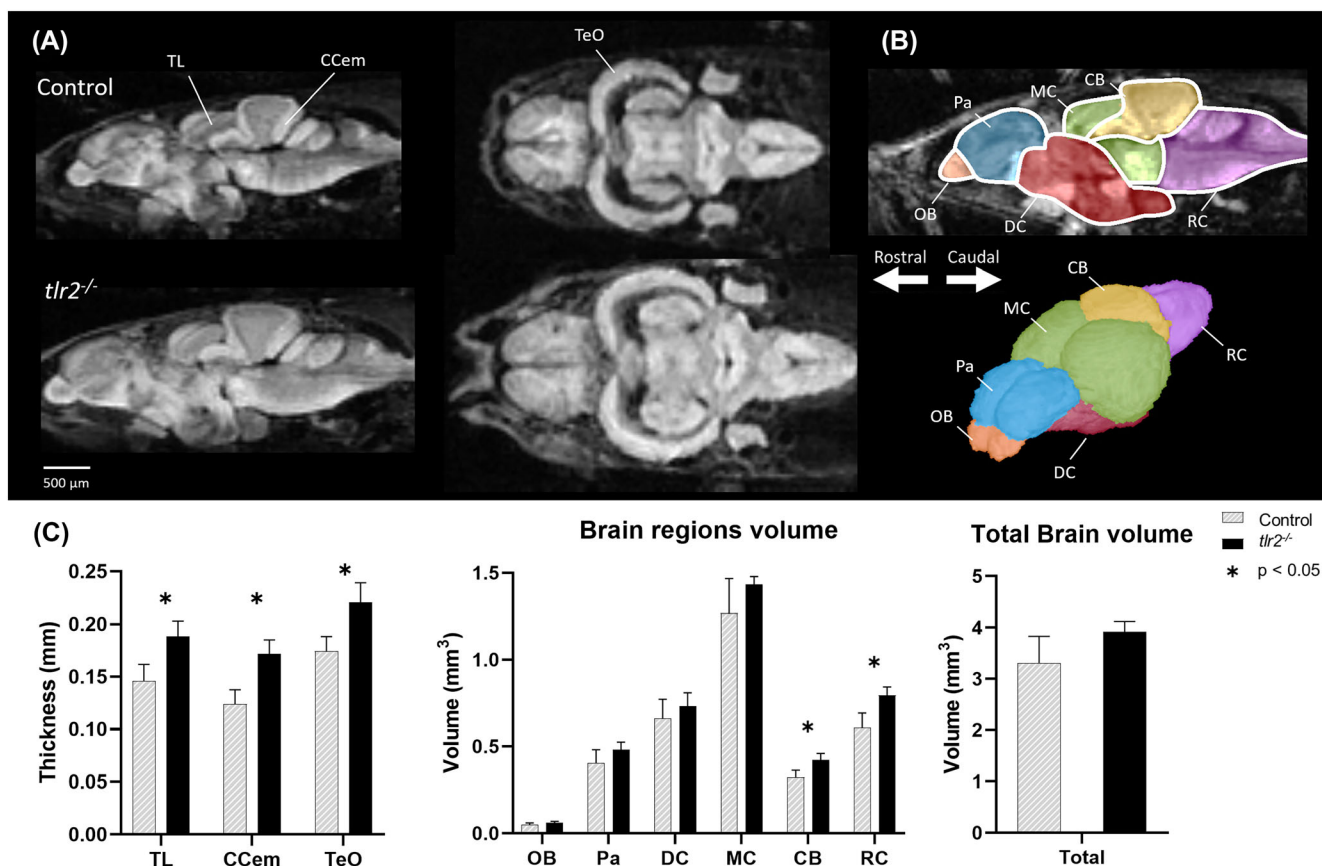
FIGURE 1   Comparison of brain structure and volume in $tlr2^{-/-}$ and control adult zebrafish. (A) Representative sagittal and coronal slices of DTI of control and $tlr2^{-/-}$ adult zebrafish obtained at 17.6 T. (B) 2D and 3D representation of the zebrafish brain, divided into its main regions, providing a comprehensive view of its anatomical organisation. (C) Comparison of the cortical thickness of the TL, the CCem and TeO shows a significant increase in $tlr2^{-/-}$ zebrafish compared with controls. Furthermore, significant increases in the volume of the CB and RC were observed. In all other brain regions, as for the total brain volume, a similar trend is observed, albeit nonsignificantly ($p > 0.05$). Acquisition details: TR 2000 ms, TE 9 ms, 4 averages, isotropic resolution 35 μm, effective b-value range of 100, 1000 or 2500 s/mm², with 4, 12 and 24 directions, respectively. Statistical analysis was performed using the unpaired t-test, assuming Gaussian distribution, with p less than 0.05 considered to imply significant differences between the control and the $tlr2^{-/-}$ group. CB, cerebellum; CCem, molecular layer of the cerebellar corpus; DC, diencephalon; DTI, diffusion tensor imaging; MC, mesencephalon; OB, olfactory bulb; Pa, pallium; RC, rhombencephalon; TeO, optic tectum; TL, longitudinal torus.

3.2 | T_2 elevation and reduced ADC underpinning cytotoxic oedema and astrogliosis in the $tlr2^{-/-}$ zebrafish brain

To zoom into microstructural changes in the zebrafish brain, we utilised T_2 and ADC measurements. Previously, quantitative T_2 and ADC measurements were used for evaluation of normal and affected brain tissue, including regular ageing, strokes, tumours and neurodegenerative diseases.[51–58] In this study, prior to conducting T_2 measurements, we examined the potential influence of magnetic field disturbances on estimated T_2 by investigating the impact of the CPMG refocusing pulse interval, as described previously.[51] The influence of pulse intervals between 6 to 18 ms on brain T_2 was negligible (see Figure S3), suggesting an insignificant impact of magnetic field disturbances on estimated T_2. In addition, the differences in T_2 times between single-slice MSME and multi-slice MSME were negligible (see Figure S3), indicating a minimal influence of magnetization transfer-related bias of the water signal.[59] Figure 2 shows T_2 and ADC changes in six areas in control and $tlr2^{-/-}$ zebrafish brain. ROIs were selected in various brain regions: the granular layer of the cerebellar corpus (CCeg), the CCem, the TL, the medial longitudinal fascicle (MLF), the diffusive nucleus of the inferior lobe (DIL) and the medial zone of the dorsal telencephalon (DM). An overall increase in the T_2 relaxation time was observed in all selected brain regions of the $tlr2^{-/-}$ zebrafish brain (Figure 2B), ranging from 17% in the DM to 28% in the CGeg. Complementary ADC analysis showed a significant reduction of the diffusivity in the CCeg, CCem and DM by 42%, 39% and 23%, respectively. Other ROIs showed a similar trend towards reduced diffusivity. The elevation in T_2, coupled with the reduction in ADC, could be an indication of elevated astrogliosis and astroglia scarring,[60,61] as documented in earlier studies for $tlr2^{-/-}$ mice.[62] Moreover, in contrast to vasogenic oedema,
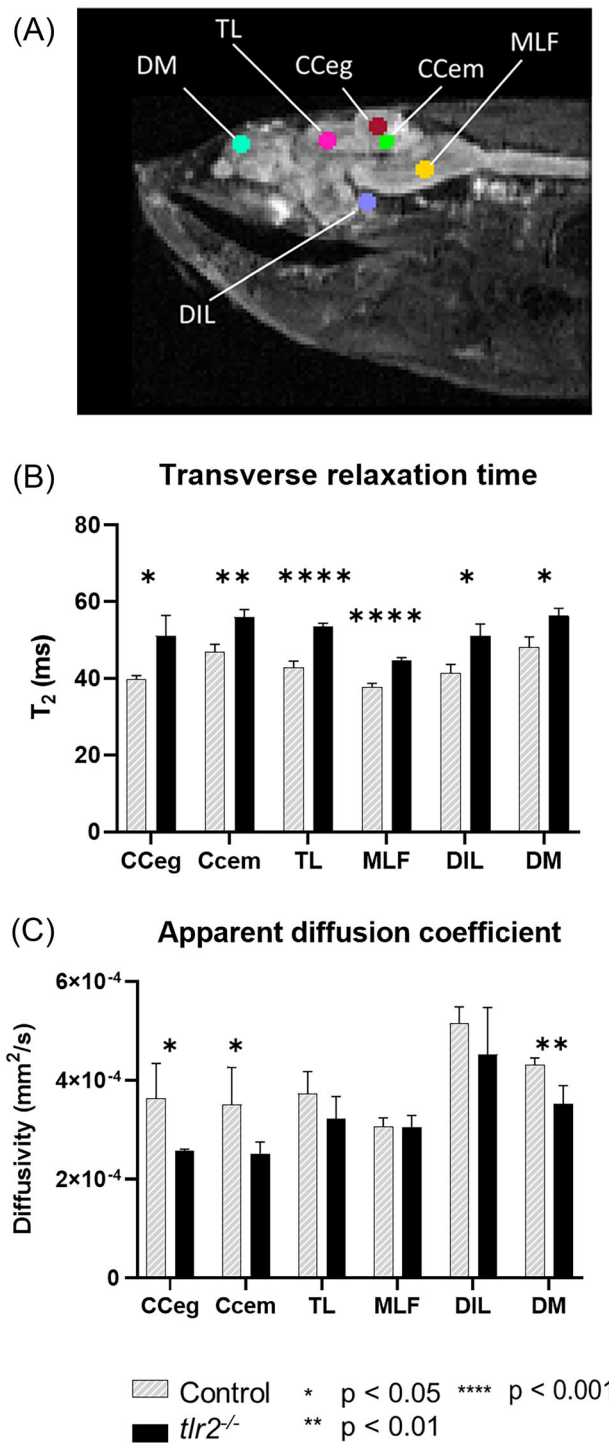
FIGURE 2 T_2 relaxation time and *ADC* measurement in various brain regions of control and *tlr2* mutant (*tlr2*$^{-/-}$) zebrafish. (A) Anatomical DWI (*b*-value 1000 s/mm^2), sagittal slice, showing ROIs used for T_2 and *ADC* estimation. (B) Estimated T_2 relaxation times in selected ROIs of control and *tlr2*$^{-/-}$ zebrafish. (C) Estimated *ADC* in selected ROIs of control and *tlr2*$^{-/-}$ zebrafish. Acquisition details for MSME: *TR* 3000, τ 6.0 ms, 4 averages, resolution 47 × 47 μm and a slice thickness of 500 μm; and for DWI: *TR* 1000 ms, *TE* 13 ms, 4 averages, resolution 47 × 47 μm, slice thickness 200 μm and effective *b*-value range 50, 500, 1000, 1500, 2000, 2500 or 3000 s/mm^2. Statistical analysis was performed using the unpaired *t*-test, assuming Gaussian distribution, with *p* less than 0.05 considered to imply significant differences between the control and the *tlr2*$^{-/-}$ group. *$p < 0.05$, **$p < 0.01$, ****$p < 0.001$. ADC, apparent diffusion coefficient; CCeg, granular layer of the cerebellar corpus; CCem, molecular layer of the cerebellar corpus; DIL, diffuse nucleus of the inferior lobe; DM, medial zone of the dorsal telencephalon; DWI, diffusion-weighted imaging; MLF, medial longitudinal fascicle; MSME, multislice multiecho; ROI, region of interest; TL, longitudinal torus.

which exhibits significant increases in diffusivity, cytotoxic oedema results in restricted diffusion and reduced ADC,[63,64] most profoundly occurring in astrocytes.[65] An increase in potential biomarkers of oedema such as aquaporin 4 (AQP4), which regulate brain water and CSF water movement, have been detected in models of neurodegeneration disease.[21] It is intriguing that an increase in cortical thickness in asymptomatic mutation carriers was reported along with a substantial reduction in the mean diffusivity, almost a decade prior to the predicted clinical onset,[48] a finding that parallels the alterations in cerebral volume and reduced diffusivity in the current study. In the present work, zebrafish were subjected to formalin fixation to mitigate degradation processes during analysis. In this context, it is noteworthy to acknowledge that formalin fixation affects relaxation times and diffusion characteristics compared with the in vivo situation.[20,66] As formalin fixation shortens T_1 relaxation times, we used relatively shorter repetition times compared with those required for in vivo studies. However, this poses a challenge when translating our methods for *in vivo* measurements, as longer repetition times would be required, consequently extending the total scan times further. Nevertheless, in the current study, to make a relevant comparison between fixed control and *tlr2*$^{-/-}$ fish, we strictly followed the same fixation protocol for both groups.

3.3 | Phasor-based multicomponent analysis reveals restricted diffusivity in the *tlr2*$^{-/-}$ zebrafish brain

To obtain further insight into the nature of the observed reduced diffusivity, multicomponent analysis of exponential *ADC* decay curves was performed by the phasor approach.[67] *ADC* is influenced by the mobility of water molecules in different tissue compartments, with each compartment exhibiting distinct *ADC* components. Several studies have shown biexponential diffusion decay in the brain, characterised by slow and fast diffusion compartments.[68–70] In this context, the slow diffusion component represents compartments within the brain that exhibit hindered diffusion, while the fast diffusion component represents compartments with relatively unrestricted diffusion. Although it has been suggested that these compartments represent intracellular and extracellular populations, there is evidence indicating that both compartments partly originate from the intracellular space.[70] The current work refers to these compartments as slow and fast diffusion components rather than intracellular and extracellular diffusivity. Here, we chose the CCem structure as our prime example for conducting a multicomponent AD analysis due to its notable alterations in T_2 and *ADC* analysis. In this context, our emphasis was on exploring the multicomponent characteristics of the *ADC* signal within affected brain tissue in *tlr2*$^{-/-}$ zebrafish. Multicomponent analysis of the *ADC* decay curve was conducted employing the phasor approach (Figure 3). Phasor data from the CCem of the *tlr2*$^{-/-}$ and control zebrafish brain demonstrated nearly complete separation (Figure 3A), indicating significant differences in the *ADC* of both groups. Figure 3B displays the monocomponent analysis of *ADC* value changes in the CCem of *tlr2*$^{-/-}$ showing that the *ADC* of *tlr2*$^{-/-}$ was significantly reduced compared with the control group, which is well in line with the results of fitting by the nonlinear least square algorithm discussed in Figure 2. The shape of the phasor data, fully separated from the semicircle, indicates a bi-component system with a slow ($0 < ADC_{slow} < 4·10^{-4}$ mm^2/s) and a fast ($4·10^{-4} < ADC_{fast} < 1·10^{-3}$ mm^2/s) *ADC* component. The phasor plot coordinates of the CCem were fitted to bi-component *ADC* systems, based on the bi-exponential fit function (Equation 3). Mean ADC_{slow} and ADC_{fast} found for the CCem of the *tlr2*$^{-/-}$ and control zebrafish by the phasor approach, as well as their area (%), are summarised in Figure 3C–E. The bi-component analysis showed a significant reduction in the absolute value of ADC_{fast}, and a substantial increase in the area of ADC_{slow}. These findings imply that diffusivity in the CCem of *tlr2*$^{-/-}$ zebrafish is primarily influenced by slow diffusion compartments to a greater extent than observed in the control group. In addition, they point to microstructural changes occurring within the fast diffusivity compartments. Various biological processes could lead to restricted diffusion. Among these, astrogliosis, cytotoxic oedema and inflammatory processes have been previously reported for *tlr2*$^{-/-}$ models, although conflicting reports are available for pro-inflammatory processes in TLR2 deficiency.[71,72] In the current work, we applied very short diffusion-encoding times that facilitated exploration of water diffusion over very short distances (micrometre regime), reducing the influence of potential interactions occurring during the application of longer diffusion times.[73] The spatial regime achieved in our work may not be currently feasible with clinical systems due to the lack of strong field gradients.

3.4 | DTI and DKI analysis reveal diminished diffusivity and enhanced kurtosis in the *tlr2*$^{-/-}$ zebrafish brain

To further evaluate potential alterations in the microstructure in the *tlr2*$^{-/-}$ zebrafish brain, DTI was utilised. DTI expands upon traditional dMRI. It enhances the understanding of structural characteristics by utilising the effects of anisotropic diffusion, accessed by measuring the diffusion-weighted MR signal in at least six different diffusion directions. These diffusion-weighted MR signals are translated into a diffusion tensor, represented as an ellipsoid model, of which the eigenvectors (ε_1, ε_2, ε_3) and eigenvalues (λ_1, λ_2, λ_3) represent the principal axis frame of the diffusion tensor and the diffusivity, respectively. Here, the eigenvectors are arranged such that $\lambda_1 \geq \lambda_2 \geq \lambda_3$. In WM structures, the diffusivity along the axons is the least restricted and represented by the largest principal eigenvalue, the axial diffusivity ($D_{\parallel}$, λ_1). The diffusivity perpendicular to the axons is represented by the average of the eigenvalues λ_2 and λ_3, the radial diffusivity ($D_{\perp}$). The mean diffusivity is estimated as the average intensity of the three eigenvectors (MD). Finally, *FA* is used to estimate the extent of the directional preference of the diffusivity, where an *FA* of

(A)

(B)

(C)

(D)

(E)

	Control		tlr2⁻/⁻	
	ADC ·10⁻⁴ (mm²/s)	Area (%)	ADC ·10⁻⁴ (mm²/s)	Area (%)
Slow component	2.8 ± 0.2	64.2 ± 2.4	2.1 ± 0.0	77.6 ± 2.4*
Fast component	8.1 ± 0.3	35.8 ± 2.4	6.8 ± 0.2*	22.4 ± 2.4*
R^2 of fit	0.9992		0.9993	
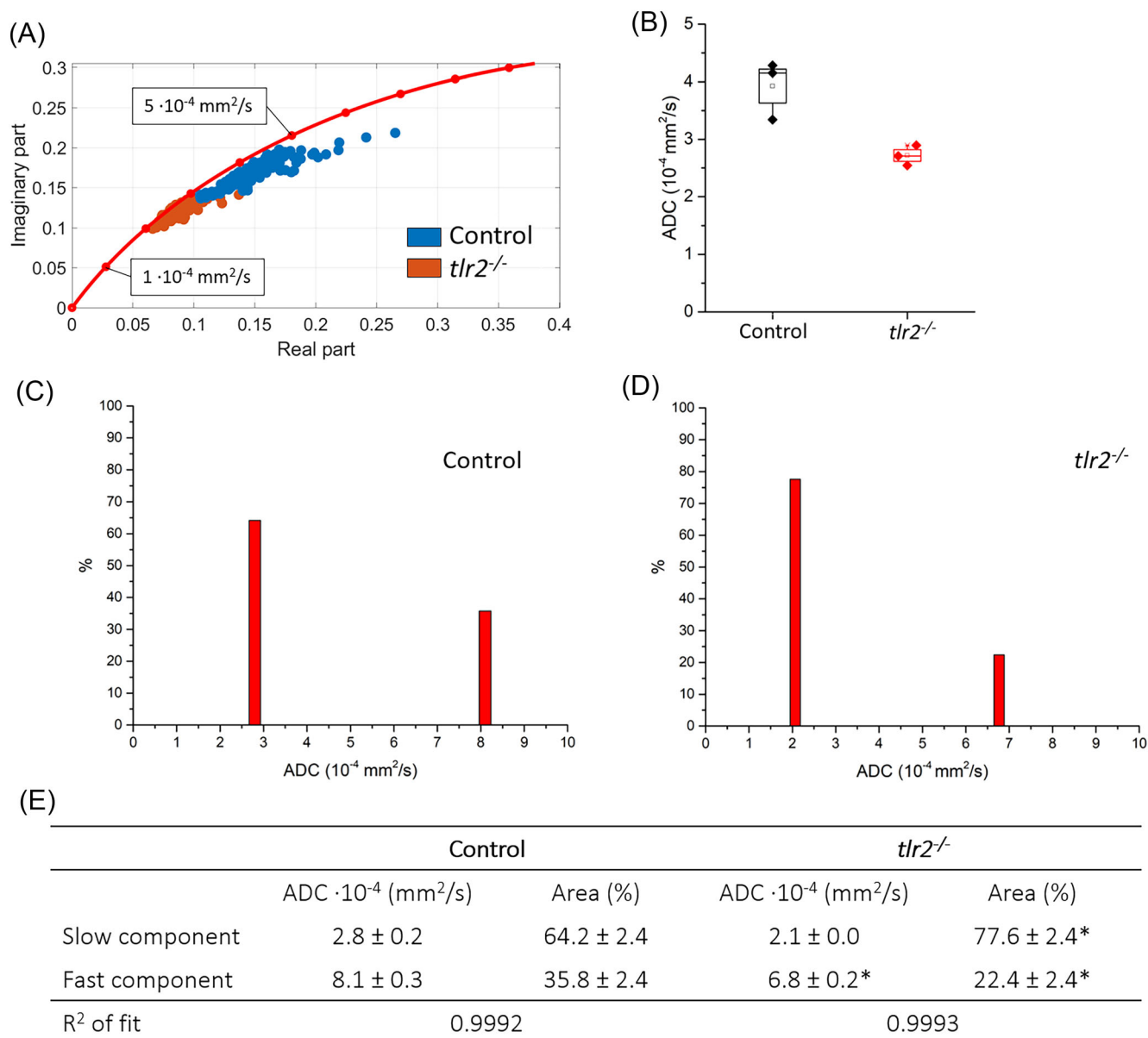
* Significant difference found from control according to two-sample t-test at 95% significance level

FIGURE 3 Phasor analysis of the experimental *ADC* curves. (A) Phasor plot of the CCem of $tlr2^{-/-}$ and control, relative to the phasor plot semicircle (red). On the semicircle, 0 mm²/s is located at [0,0], with steps of $1 \cdot 10^{-4}$ mm²/s indicated as red dots on the semicircle. (B) Monocomponent analysis shows that the *ADC* in $tlr2^{-/-}$ is significantly reduced, while (C–E) Multicomponent analysis of the *ADC* decay curve in the CCem shows a significant increase in the area of the slow diffusion component in $tlr2^{-/-}$, associated with restricted diffusion. Acquisition details for the DWI used for phasor plot analysis: *TR* 1000 ms, *TE* 13 ms, 4 averages, resolution 47 × 47 μm, slice thickness 200 μm and effective b-value range 50, 500, 1000, 1500, 2000, 2500 or 3000 s/mm². Statistical analysis was performed using the unpaired t-test, assuming Gaussian distribution, with p less than 0.05 considered to imply significant differences between the control and the $tlr2^{-/-}$ group. * $p < 0.05$. ADC, apparent diffusion coefficient; CCem, molecular layer of the cerebellar corpus; DWI, diffusion-weighted imaging.

0 indicated full isotropic diffusivity and an *FA* of 1 indicated full anisotropic diffusivity. In the current study, DTI data were used to generate $D_{\parallel}$, $D_{\perp}$, *MD* and *FA* maps (Figure 4A) and to estimate the mean $D_{\parallel}$, $D_{\perp}$, *MD* and *FA* of major brain regions (Figure 4C).

Differences in $D_{\parallel}$, $D_{\perp}$ and *MD* in the major brain region were found to be negligible, although a robust and consistent trend towards decreased $D_{\parallel}$, $D_{\perp}$ and *MD* was observed, aligning closely with the reduced *ADC* found by DWI and previous reports.[10] Notably, *FA* exhibited a significant reduction in the Pa and MC, in line with earlier observations for $tlr2^{-/-}$ mice.[11] In other brain regions, a similar tendency towards reduced *FA* was consistently observed in $tlr2^{-/-}$ zebrafish relative to the control group, albeit nonsignificant.
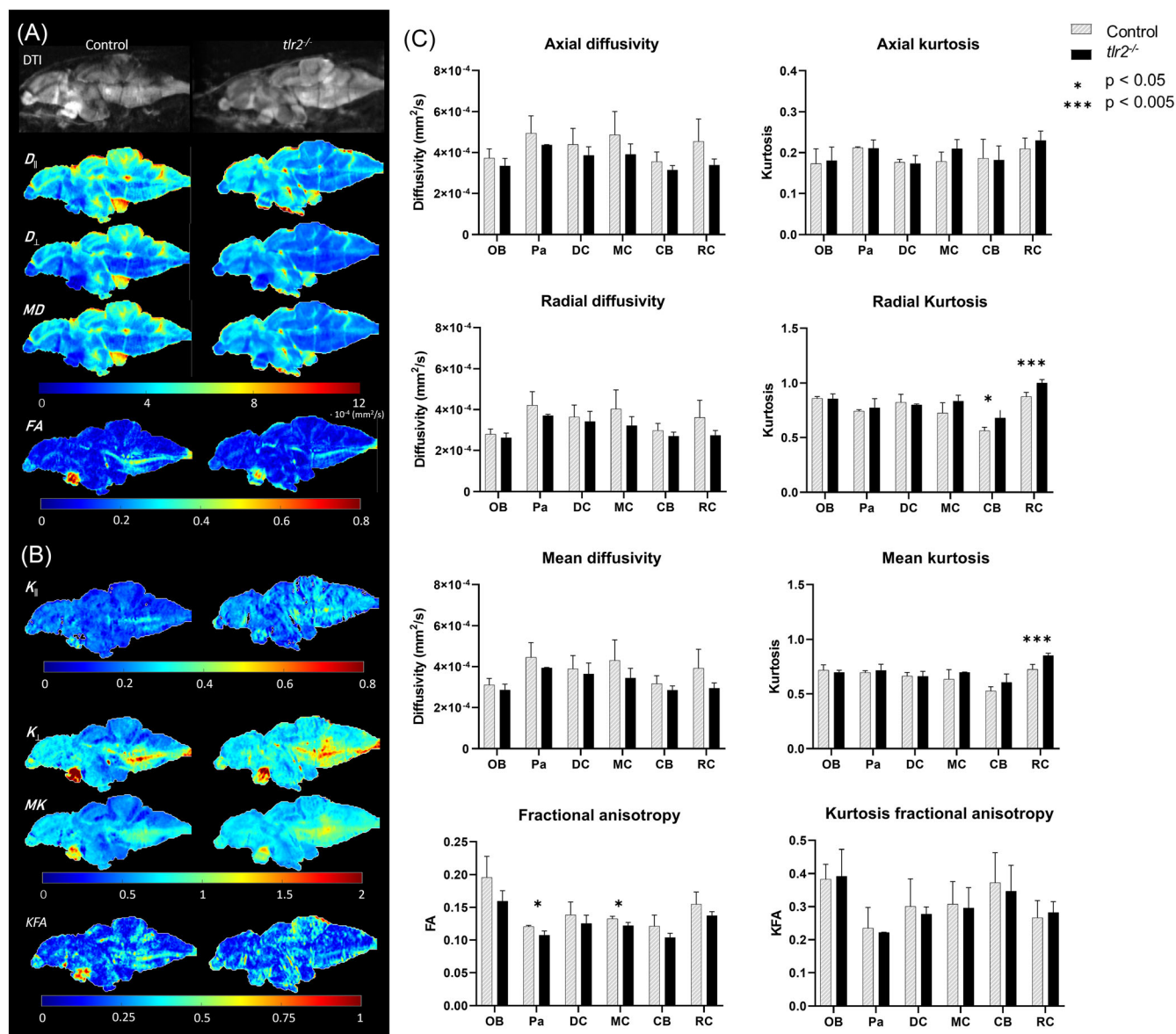
FIGURE 4 Comparison of DTI results in the main brain regions of $tlr2^{-/-}$ and control adult zebrafish. Representative central slice of DTI measurements of control and $tlr2^{-/-}$ adult zebrafish. (A) From these slices, the diffusion tensor metrics were estimated: $D_{\parallel}$, $D_{\perp}$, MD and FA, as well as (B) the diffusion kurtosis metrics: $K_{\parallel}$, $K_{\perp}$, MK and KFA. (C) DTI and DKI results of $tlr2^{-/-}$ adult zebrafish compared with controls reveal a noteworthy trend towards decreased $D_{\parallel}$, $D_{\perp}$ and MD, reduced FA, as well as increased $K_{\parallel}$, $K_{\perp}$ and MK. Additionally, a significant decrease in KFA is observed in the $tlr2^{-/-}$ group. Acquisition details: TR 2000 ms, TE 12.4 ms, 32 averages, resolution $25 \times 25 \times 200$ µm, effective b-value range 4, 1000, 3500 or 6000 s/mm², with 8, 12, 24 or 36 directions, respectively. Statistical analysis was performed using the unpaired t-test, assuming Gaussian distribution, with p less than 0.05 considered to imply significant differences between the control and the $tlr2^{-/-}$ group. *$p < 0.05$, ***$p < 0.005$. CB, cerebellum; $D_{\parallel}$, axial diffusivity; $D_{\perp}$, radial diffusivity; DC, diencephalon; DKI, diffusion kurtosis imaging; DTI, diffusion tensor imaging; FA, fractional anisotropy; $K_{\parallel}$, axial kurtosis; $K_{\perp}$, radial kurtosis; KFA, kurtosis fractional anisotropy; MC, mesencephalon; MD, mean diffusivity; MK, mean kurtosis; OB, olfactory bulb; Pa, pallium; RC, rhombencephalon.

Further insight was obtained by employing DKI. DWI and DTI rely on the assumption that diffusivity (in the brain) follows a Gaussian distribution, thus simplifying the true complexity of diffusivity in the brain.[74] Considering these limitations, DKI is an extended dMRI technique for the characterisation of non-Gaussian diffusion, describing the kurtosis of the diffusion distribution. To quantify kurtosis, application of higher b-values is required, as the diffusion signal is mostly influenced by Gaussian diffusion at lower b-values.[75] In our findings, we observe the emergence of kurtosis effects at b-values exceeding 2000 s/mm², and it is increasing at larger b-values (see Figure S4). DKI data were used to generate $K_{\parallel}$, $K_{\perp}$, MK and KFA maps (Figure 4B) and to estimate the mean $K_{\parallel}$, $K_{\perp}$, MK and KFA of major brain regions (Figure 4C). We observed a significant increase in $K_{\perp}$ in the RC and CB, and a significant increase in the MK of the RC of $tlr2^{-/-}$ zebrafish compared with the control group. Elevated diffusion

kurtosis signifies a greater departure from the Gaussian distribution of water molecule diffusion, suggesting an elevated degree of diffusion restriction. These findings are in full agreement with our monocomponent and multicomponent analysis of the *ADC* signal, indicating strongly restricted diffusion.

In general, the diffusion metrics $D_\parallel$ and $D_\perp$ are indicative of myelin integrity and axonal damage, *MD* is associated with oedema and proliferation of cells in neoplastic growth, and *FA* serves as a highly sensitive biomarker for assessing the integrity of WM. In this context, diminished *FA* was related to the loss of neurons, myelin swellings and severe cytotoxic oedema, and reduced *MD* was related to glial cell death and loss.[76] Regarding kurtosis metrics, $K_\parallel$ is particularly responsive to intracellular structures, whereas $K_\perp$ is influenced by alterations in cellular membranes and myelin layers. *MK*, on the other hand, is more broadly linked to the microstructural complexity of the brain. An increase in *MK* may be associated with denser cell packing or greater cellular complexity, while a decrease in *MK* may be attributed to a loss of cellular structure.[74] Moreover, diffusion kurtosis metrics provide some advantages over diffusion tensor metrics for their increased sensitivity for isotropic GM.[77]

Based on our findings in 3-month-old $tlr2^{-/-}$ zebrafish, when compared with a control group, we observed several changes in brain metrics. These include an increase in brain volume, strong T_2 signals, reduced *ADC*, restricted diffusivity and alterations in various diffusion tensor and diffusion kurtosis metrics, such as diminished $D_\parallel$, $D_\perp$, *MD* and *FA*, coupled with an increase in $K_\parallel$, $K_\perp$ and *MK*. Demyelination is typically associated with increased $D_\perp$, unadjusted $D_\parallel$, reduced *FA* and decreased $K_\perp$ and *MK*.[78–80] Reactive astrogliosis was previously found to lead to decreased $D_\parallel$, stable $D_\perp$, reduced *MD*, increased *FA* and increased *MK*.[81,82] Our findings suggest axonal degeneration or cytotoxic oedema within the analysed brain regions. For axonal degeneration, reduced $D_\parallel$, $D_\perp$ and *FA* were reported, with an apparent increase of kurtosis.[79,83–85] A decrease in diffusivity ($D_\parallel$, $D_\perp$, *MD*), decrease in *FA* and increase in kurtosis ($K_\parallel$, $K_\perp$, *MK*) was previously observed in early hypoxic–ischaemic brain oedema.[86]

We conducted an examination to assess the impact of *b*-value dependency on the reliability of estimated diffusion tensor and diffusion kurtosis metrics. Our study extends previous research conducted in single- and double-shell DTI and DKI measurements,[87] whereas we employed triple-shell DTI and DKI at ultrahigh magnetic field strengths (see Figure S5). Upon analysis, we observed that the majority of diffusion tensor and diffusion kurtosis metrics did not exhibit a significant shift in response to significant changes in the *b*-value range. This suggests that the majority of diffusion tensor and diffusion kurtosis metrics, obtained at ultrahigh magnetic fields and with four distinct *b*-values (b_0 included), are robust and relatively unaffected by variations in the *b*-value range. Based on these findings, we conclude that future studies with somewhat similar *b*-value ranges may therefore find our data a valuable reference point.

3.5 | Genomic deletion of TLR2 signifies compromised integrity in white matter tracks

Subsequently, we investigated the effect of genomic deletion of TLR2 on WM integrity in adult zebrafish by DTI. Seven WM structures were identified and localised in the zebrafish brain using dMRI tractography by stTDI CSD (Figure 5A): the posterior commissure (Cpost), the commissure of the secondary gustatory nuclei (Cgus), the ansulate commissure (Cans), the ventral rhombencephalic commissure (Cven), the MLF, the optic tract (OT) and the lateral longitudinal fascicle (LLF). The integrity of these WM structures was monitored by comparing DTI and DKI metrics. Significantly lower $D_\parallel$, *MD* and *FA* were observed in the Cven of $tlr2^{-/-}$ zebrafish, along with increased $K_\parallel$, $K_\perp$, *MK* and *FKA*. In the Cgus, we observed a significantly lower *FA* and increased $K_\perp$. In addition, the Cpost showed reduced $D_\parallel$ and *MD*, with increased $K_\perp$; the MLF showed increased $K_\perp$; and for the LLF, reduced $D_\parallel$, $D_\perp$ and *MD*, in combination with increased $K_\perp$ and *MK*. Overall, DTI and DKI data of WM structures in $tlr2^{-/-}$ zebrafish show a consistent trend of reduced diffusivity ($D_\parallel$, $D_\perp$ and *MD*) and *FA* across most WM structures. Moreover, we observed a trend indicating increased kurtosis ($K_\parallel$, $K_\perp$ and *MK*) and *KFA* when compared with the control group. Previously, increased kurtosis, in combination with decreased diffusivity levels and reduced *FA*, have been attributed to microstructural changes in the brain. APP/PS1 Alzheimer's disease mouse models show a significant increase in kurtosis in the hippocampus, cortex and thalamus, linked to a significant increase in amyloid beta (Aβ) plaque loads.[88] A longitudinal report of the same pathological model showed similar observations, including significant drops in *FA* in various brain regions.[89] It has been suggested that TLR2 plays a significant role in clearing toxic Aβ, as shown in an APP Alzheimer's disease mouse model.[90] Another observation made in $tlr2^{-/-}$ mouse models was increased astrogliosis and demyelination in WM structures.[62] On the other hand, cuprizone-induced demyelination and inflammation reduced $K_\parallel$, $K_\perp$ and *MK* in the cortex and corpus callosum,[80] contrary to the observations in the current study. Increased mean kurtosis was reported as a potential biomarker of reactive astrogliosis, although the same report did not see any significant alterations in *FA* or MD.[82]

Our analysis has revealed compelling evidence of a compromise in the integrity of various WM structures within the brain of $tlr2^{-/-}$ zebrafish. The alterations of the neural architecture suggest a potential link to neurobehavioural changes observed in other $tlr2^{-/-}$ models. Here, we found evidence for microstructural changes in the Cven, a bundle of nerves carrying signals between the two halves of the hind brain. These signals originate from different parts of the brain, including the sensory area for touch and balance, as well as groups of cells related to sensing and moving.[91] Lampreys (*Lampetra fluviatilis*), with a transected Cven exhibited compromised spontaneous locomotion and altered movements,[91] illustrating the role played by the Cven in orchestrating and regulating these motor behaviours. These observations are consistent with the
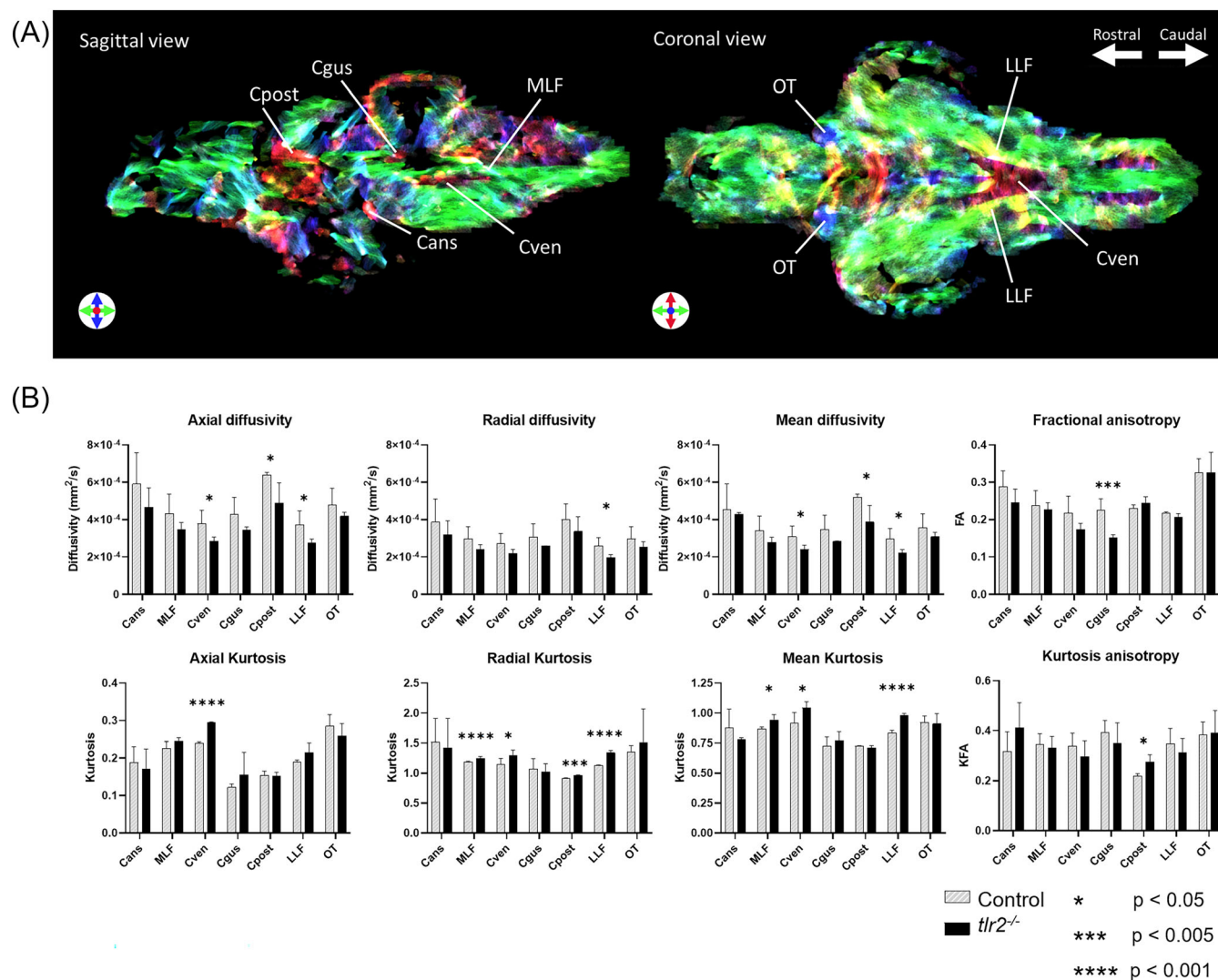
FIGURE 5 Comparison of DTI results of white matter structures of $tlr2^{-/-}$ and control adult zebrafish. (A) Sagittal and coronal slices of the DEC stTDI msmt-CSD map, used for the identification of white matter structures in the zebrafish brain. Acquisition details: TR 2000 ms, TE 9 ms, 4 averages, isotropic resolution 35 μm, effective b-value range 100, 1000 or 2500 s/mm^2, with 4, 12 and 24 directions, respectively. (B) Diffusion metrics estimated by DTI results show reduced $D_{\parallel}$, $D_{\perp}$ and MD, reduced FA, increased $K_{\parallel}$, $K_{\perp}$ and MK and KFA in white matter structures in the $tlr2^{-/-}$ zebrafish brain. Acquisition details: TR 2000 ms, TE 12.4 ms, 32 averages, resolution $25 \times 25 \times 200$ μm, effective b-value range 4, 1000, 3500 or 6000 s/mm^2, with 8, 12, 24 or 36 directions, respectively. Statistical analysis was performed using the unpaired t-test, assuming Gaussian distribution, with p less than 0.05 considered to imply significant differences between the control and the $tlr2^{-/-}$ group. *$p < 0.05$, ***$p < 0.005$, ****$p < 0.001$. Cans, ansulate commissure; Cgus, commissure of the secondary gustatory nuclei; Cpost, posterior commissure; CSD, constraint spherical deconvolution; Cven, ventral rhombencephalic commissure; $D_{\parallel}$, axial diffusivity; $D_{\perp}$, radial diffusivity; DEC, directional encoded colour; DTI, diffusion tensor imaging; FA, fractional anisotropy; $K_{\parallel}$, axial kurtosis; $K_{\perp}$, radial kurtosis; KFA, kurtosis fractional anisotropy; LLF, lateral longitudinal fascicle; MD, mean diffusivity; MK, mean kurtosis; MLF, medial longitudinal fascicle; msmt, multishell multitissue; OT, optic tract; stTDI, short-track track-density imaging.

diminished spontaneous activity observed in $tlr2^{-/-}$ mice.[11] Our insight into microstructural alterations in the Cven of $tlr2^{-/-}$ zebrafish sheds light on this phenomenon. Parallel to the Cven, the Cgus was found to be affected in $tlr2^{-/-}$ zebrafish. The Cgus is the neural pathway connecting the secondary gustatory nuclei present on both sides of the zebrafish brain, which are involved in processing taste-related information as part of the gustatory system.[92] Our observations in microstructural changes in the Cgus could contribute to explaining previous observations in $tlr2^{-/-}$ mice showing diminished food consumption,[93] as disrupted communication with the secondary gustatory nuclei might lead to difficulties in processing and perceiving taste sensation. The Cpost is a diencephalic nerve bundle that is involved in facilitating communication with the pretectal nuclei,[30] and is involved in visual processing, circadian rhythms and motor control.[94] Previous studies showed disrupted circadian rhythms in $tlr2^{-/-}$ mice,[93] to which our observations might provide further insights.

4 | CONCLUSION AND FUTURE OUTLOOK

In summary, our study unveils the impact of genomic TLR2 deletion in zebrafish, leading to microstructural alterations within diverse brain tissues. Applying dMRI at ultrahigh magnetic fields provided the necessary SNR and contrast that has enabled us to discriminate and characterise major brain regions as well as specific WM structures, thereby unravelling the microstructural changes associated with $tlr2^{-/-}$ zebrafish. Distinct dMRI techniques provided a diverse array of diffusion metrics, each offering a unique perspective into the architectural framework and transformations occurring in the pathological model. Notably, our study showed significant changes in the diffusivity and kurtosis profiles of multiple WM structures, which mirror neurobehavioural shifts observed in $tlr2^{-/-}$ models. These findings contribute an additional layer of insight to improve our understanding of the origin of these behavioural changes.

In future, to extrapolate our results to a broader context, research should prioritise replicating these findings with a larger sample size, encompassing both male and female zebrafish across various age groups, including older fish. This approach will facilitate more robust statistical analyses and a thorough exploration of potential variables and interactions. Furthermore, techniques such as histological staining and spectroscopic methods, including localised spectroscopy and high-resolution magic angle spinning, could offer further insight towards an increased understanding of the precise microstructural and metabolic changes in the brain of $tlr2^{-/-}$ models.

In essence, our research provides insight into the relationship between TLR2 and the microstructural architecture of the brain. Especially, our utilisation of diffusion MRI at ultrahigh magnetic fields signifies a substantial advancement, finally providing the required foundation for investigating these relationships in the tiny zebrafish brain.

AUTHOR CONTRIBUTIONS

Rico Singer, A. Alia and Herman P. Spaink designed the experiments. Rico Singer and Ina Oganezova conducted MRI experiments. Wanbin Hu and Yi Ding prepared zebrafish breading and samples. Rico Singer and A. Alia analysed the results. Huub J. M. de Groot, Herman P. Spaink and A. Alia supervised the project. Rico Singer and A. Alia wrote the manuscript. All authors reviewed the manuscript.

CONFLICT OF INTEREST STATEMENT

The authors declare no conflicts of interest.

DATA AVAILABILITY STATEMENT

All relevant data are within the paper and its supplementary information file.

ORCID

A. Alia 🆔 https://orcid.org/0000-0002-4900-9749

REFERENCES

1. Li D, Wu M. Pattern recognition receptors in health and diseases. *Signal Transduct Target Ther*. 2021;6(1):291. doi:10.1038/s41392-021-00687-0
2. Hu W, Spaink HP. The role of TLR2 in infectious diseases caused by mycobacteria: from cell biology to therapeutic target. *Biology*. 2022;11(2):246. doi:10.3390/biology11020246
3. Sameer AS, Nissar S. Toll-like receptors (TLRs): structure, functions, signaling, and role of their polymorphisms in colorectal cancer susceptibility. *Biomed Res Int*. 2021;2021:1157023. doi:10.1155/2021/1157023
4. Behzadi P, Garcia-Perdomo HA, Karpinski TM. Toll-like receptors: general molecular and structural biology. *J Immunol Res*. 2021;2021:9914854. doi:10.1155/2021/9914854
5. Meijer AH, Gabby Krens SF, Medina Rodriguez IA, et al. Expression analysis of the Toll-like receptor and TIR domain adaptor families of zebrafish. *Mol Immunol*. 2004;40(11):773-783. doi:10.1016/j.molimm.2003.10.003
6. Oliveira-Nascimento L, Massari P, Wetzler LM. The role of TLR2 in infection and immunity. *Front Immunol*. 2012;3:79. doi:10.3389/fimmu.2012.00079
7. Dasu MR, Thangappan RK, Bourgette A, DiPietro LA, Isseroff R, Jialal I. TLR2 expression and signaling-dependent inflammation impair wound healing in diabetic mice. *Lab Investig*. 2010;90(11):1628-1636. doi:10.1038/labinvest.2010.158
8. Marks KE, Cho K, Stickling C, Reynolds JM. Toll-like receptor 2 in autoimmune inflammation. *Immune Netw*. 2021;21(3):e18. doi:10.4110/in.2021.21.e18
9. Pascual M, Calvo-Rodriguez M, Núñez L, Villalobos C, Ureña J, Guerri C. Toll-like receptors in neuroinflammation, neurodegeneration, and alcohol-induced brain damage. *IUBMB Life*. 2021;73(7):900-915. doi:10.1002/iub.2510

10. McDonald CL, Hennessy E, Rubio-Araiz A, et al. Inhibiting TLR2 activation attenuates amyloid accumulation and glial activation in a mouse model of Alzheimer's disease. *Brain Behav Immun.* 2016;58:191-200. doi:10.1016/j.bbi.2016.07.143

11. Zhou C, Sun X, Hu Y, et al. Genomic deletion of TLR2 induces aggravated white matter damage and deteriorated neurobehavioral functions in mouse models of Alzheimer's disease. *Aging.* 2019;11(17):7257-7273. doi:10.18632/aging.102260

12. Hu Y, Sun X, Wang S, et al. Toll-like receptor-2 gene knockout results in neurobehavioral dysfunctions and multiple brain structural and functional abnormalities in mice. *Brain Behav Immun.* 2021;91:257-266. doi:10.1016/j.bbi.2020.10.004

13. van Schadewijk R, Krug JR, Shen D, et al. Magnetic resonance microscopy at cellular resolution and localised spectroscopy of *Medicago truncatula* at 22.3 Tesla. *Sci Rep.* 2020;10(1):971. doi:10.1038/s41598-020-57861-7

14. Kabli S, Alia A, Spaink HP, Verbeek FJ, De Groot HJ. Magnetic resonance microscopy of the adult zebrafish. *Zebrafish.* 2006;3(4):431-439. doi:10.1089/zeb.2006.3.431

15. Kabli S, Spaink HP, De Groot HJ, Alia A. In vivo metabolite profile of adult zebrafish brain obtained by high-resolution localized magnetic resonance spectroscopy. *J Magn Reson Imaging.* 2009;29(2):275-281. doi:10.1002/jmri.21609

16. Haud N, Kara F, Diekmann S, et al. rnaset2 mutant zebrafish model familial cystic leukoencephalopathy and reveal a role for RNase T2 in degrading ribosomal RNA. *Proc Natl Acad Sci USA.* 2011;108(3):1099-1103. doi:10.1073/pnas.1009811107

17. Ramirez IB, Pietka G, Jones DR, et al. Impaired neural development in a zebrafish model for Lowe syndrome. *Hum Mol Genet.* 2012;21(8):1744-1759. doi:10.1093/hmg/ddr608

18. Kabli S, He S, Spaink HP, et al. In vivo magnetic resonance imaging to detect malignant melanoma in adult zebrafish. *Zebrafish.* 2010;7(2):143-148. doi:10.1089/zeb.2009.0649

19. Eeza MNH, Singer R, Ding Y, et al. Probing microstructural changes in muscles of leptin-deficient zebrafish by non-invasive ex-vivo magnetic resonance microimaging. *PLoS ONE.* 2023;18(4):e0284215. doi:10.1371/journal.pone.0284215

20. Hamilton N, Allen C, Reynolds S. Longitudinal MRI brain studies in live adult zebrafish. *NMR Biomed.* 2023;36(7):e4891. doi:10.1002/nbm.4891

21. Gatto RG, Amin MY, Deyoung D, Hey M, Mareci TH, Magin RL. Ultra-high field diffusion MRI reveals early axonal pathology in spinal cord of ALS mice. *Transl Neurodegener.* 2018;7(1):20. doi:10.1186/s40035-018-0122-z

22. Gatto RG, Wu YC. Editorial: innovative imaging techniques in preclinical models of neurodegenerative diseases. *Front Neurosci.* 2021;15:801037. doi:10.3389/fnins.2021.801037

23. Ullmann JF, Calamante F, Collin SP, Reutens DC, Kurniawan ND. Enhanced characterization of the zebrafish brain as revealed by super-resolution track-density imaging. *Brain Struct Funct.* 2015;220(1):457-468. doi:10.1007/s00429-013-0667-7

24. Hu W, Yang S, Shimada Y, et al. Infection and RNA-seq analysis of a zebrafish tlr2 mutant shows a broad function of this toll-like receptor in transcriptional and metabolic control and defense to Mycobacterium marinum infection. *BMC Genomics.* 2019;20(1):878. doi:10.1186/s12864-019-6265-1

25. Hu W, van Steijn L, Li C, et al. A novel function of TLR2 and MyD88 in the regulation of leukocyte cell migration behavior during wounding in zebrafish larvae. *Front Cell Dev Biol.* 2021;9:624571. doi:10.3389/fcell.2021.624571

26. Iglesias JE, Crampsie S, Strand C, Tachrount M, Thomas DL, Holton JL. Effect of fluorinert on the histological properties of formalin-fixed human brain tissue. *J Neuropathol Exp Neurol.* 2018;77(12):1085-1090. doi:10.1093/jnen/nly098

27. Carr HY, Purcell EM. Effects of diffusion on free precession in nuclear magnetic resonance experiments. *Phys Rev.* 1954;94(3):630-638. doi:10.1103/PhysRev.94.630

28. Stejskal EO, Tanner JE. Spin diffusion measurements: spin echoes in the presence of a time-dependent field gradient. *J Chem Phys.* 1965;42(1):288-292. doi:10.1063/1.1695690

29. Kenney JW, Steadman PE, Young O, et al. A 3D adult zebrafish brain atlas (AZBA) for the digital age. *elife.* 2021;10:e69988.

30. Wullimann MF, Rupp B, Reichert H. *Neuroanatomy of the Zebrafish Brain: A Topological Atlas.* Birkhäuser Verlag; 1996. doi:10.1007/978-3-0348-8979-7

31. Haynes EM, Ulland TK, Eliceiri KW. A model of discovery: the role of imaging established and emerging non-mammalian models in neuroscience. *Front Mol Neurosci.* 2022;15:867010. doi:10.3389/fnmol.2022.867010

32. read_2dseq: quickly reads Bruker's 2dseq MRI images v. 1.0.1. MathWorks, MATLAB Central File Exchange; 2020.

33. Milford D, Rosbach N, Bendszus M, Heiland S. Mono-exponential fitting in T2-relaxometry: relevance of offset and first echo. *PLoS ONE.* 2015;10(12): e0145255. doi:10.1371/journal.pone.0145255

34. Tournier JD, Smith R, Raffelt D, et al. MRtrix3: a fast, flexible and open software framework for medical image processing and visualisation. *NeuroImage.* 2019;202:116137. doi:10.1016/j.neuroimage.2019.116137

35. Kellner E, Dhital B, Kiselev VG, Reisert M. Gibbs-ringing artifact removal based on local subvoxel-shifts. *Magn Reson Med.* 2016;76(5):1574-1581. doi:10.1002/mrm.26054

36. Veraart J, Fieremans E, Novikov DS. Diffusion MRI noise mapping using random matrix theory. *Magn Reson Med.* 2016;76(5):1582-1593. doi:10.1002/mrm.26059

37. Collier Q. Robust estimation of diffusion tensor and diffusion kurtosis imaging parameters. PhD thesis. Universiteit Antwerpen; 2018.

38. Basser PJ, Mattiello J, Lebihan D. Estimation of the effective self-diffusion tensor from the NMR spin echo. *J Magn Reson B.* 1994;8(3):247-254. doi:10.1006/jmrb.1994.1037

39. Veraart J, Sijbers J, Sunaert S, Leemans A, Jeurissen B. Weighted linear least squares estimation of diffusion MRI parameters: strengths, limitations, and pitfalls. *NeuroImage.* 2013;81:335-346. doi:10.1016/j.neuroimage.2013.05.028

40. Hansen B, Jespersen SN. Kurtosis fractional anisotropy, its contrast and estimation by proxy. *Sci Rep.* 2016;6(1):23999. doi:10.1038/srep23999

41. Tabesh A, Jensen JH, Ardekani BA, Helpern JA. Estimation of tensors and tensor-derived measures in diffusional kurtosis imaging. *Magn Reson Med.* 2011;65(3):823-836. doi:10.1002/mrm.22655

42. Hansen B, Jespersen SN. Recent developments in fast kurtosis imaging. *Front Phys.* 2017;5:1-15. doi:10.3389/fphy.2017.00040

43. Dhollander T, Raffelt D, Mito R, Connelly A. Improved white matter response function estimation for 3-tissue constrained spherical deconvolution. Conference Paper. May 2019. 27th International Society of Magnetic Resonance in Medicine; Montréal, Québec, Canada; Proceedings of the International Society for Magnetic Resonance in Medicine Volume, 27(555).

44. Jeurissen B, Tournier JD, Dhollander T, Connelly A, Sijbers J. Multi-tissue constrained spherical deconvolution for improved analysis of multi-shell diffusion MRI data. *NeuroImage.* 2014;103:411-426. doi:10.1016/j.neuroimage.2014.07.061

45. Tournier JD, Calamante F, Connelly A. MRtrix: Diffusion tractography in crossing fiber regions. *Int J Imaging Syst Technol.* 2012;22(1):53-66. doi:10.1002/ima.22005

46. Calamante F, Tournier JD, Jackson GD, Connelly A. Track-density imaging (TDI): super-resolution white matter imaging using whole-brain track-density mapping. *NeuroImage.* 2010;53(4):1233-1243. doi:10.1016/j.neuroimage.2010.07.024

47. Bohacek I, Cordeau P, Lalancette–Hébert M, et al. Toll-like receptor 2 deficiency leads to delayed exacerbation of ischemic injury. *J Neuroinflammation.* 2012;9(1):17. doi:10.1186/1742-2094-9-191

48. Fortea J, Sala-Llonch R, Bartrés-Faz D, et al. Increased cortical thickness and caudate volume precede atrophy in PSEN1 mutation carriers. *J Alzheimers Dis.* 2010;22(3):909-922. doi:10.3233/JAD-2010-100678

49. Espeseth T, Westlye LT, Fjell AM, Walhovd KB, Rootwelt H, Reinvang I. Accelerated age-related cortical thinning in healthy carriers of apolipoprotein E epsilon 4. *Neurobiol Aging.* 2008;29(3):329-340. doi:10.1016/j.neurobiolaging.2006.10.030

50. Kang K, Han J, Lee SW, et al. Abnormal cortical thickening and thinning in idiopathic normal-pressure hydrocephalus. *Sci Rep.* 2020;10(1):21213. doi:10.1038/s41598-020-78067-x

51. Roy U, Heredia-Muñoz MT, Stute L, et al. Degeneration of the suprachiasmatic nucleus in an Alzheimer's disease mouse model monitored by in vivo magnetic resonance relaxation measurements and immunohistochemistry. *J Alzheimers Dis.* 2019;69(2):363-375. doi:10.3233/JAD-190037

52. Kara F, Chen F, Ronen I, de Groot HJM, Matysik J, Alia A. In vivo measurement of transverse relaxation time in the mouse brain at 17.6 T. *Magn Reson Med.* 2013;70(4):985-993. doi:10.1002/mrm.24533

53. Ndengera M, Delattre BMA, Scheffler M, Lövblad KO, Meling TR, Vargas MI. Relaxation time of brain tissue in the elderly assessed by synthetic MRI. *Brain Behav.* 2022;12(1):e2449. doi:10.1002/brb3.2449

54. Gideon P, Thomsen C, Henriksen O. Increased self-diffusion of brain water in normal aging. *J Magn Reson Imaging.* 1994;4(2):185-188. doi:10.1002/jmri.1880040216

55. Knight MJ, Damion RA, McGarry BL, et al. Determining T2 relaxation time and stroke onset relationship in ischaemic stroke within apparent diffusion coefficient-defined lesions. A user-independent method for quantifying the impact of stroke in the human brain. *Biomed Spectrosc. Imaging.* 2019; 8(1-2):11-28. doi:10.3233/bsi-190185

56. McGarry BL, Damion RA, Chew I, et al. A comparison of T(2) relaxation-based MRI stroke timing methods in hyperacute ischemic stroke patients: a pilot study. *J Cent Nerv Syst Dis.* 2020;12:1179573520943314. doi:10.1177/1179573520943314

57. Chatel M, Darcel F, Certaines de J, Benoist L, Bernard AM. T1 and T2 proton nuclear magnetic resonance (N.M.R.) relaxation times in vitro and human intracranial tumours. *J Neuro-Oncol.* 1986;3(4):315-321. doi:10.1007/BF00165579

58. Maier SE, Sun Y, Mulkern RV. Diffusion imaging of brain tumors. *NMR Biomed.* 2010;23(7):849-864. doi:10.1002/nbm.1544

59. Radunsky D, Blumenfeld-Katzir T, Volovyk O, et al. Analysis of magnetization transfer (MT) influence on quantitative mapping of T(2) relaxation time. *Magn Reson Med.* 2019;82(1):145-158. doi:10.1002/mrm.27704

60. Lee D, Thaler JP, Berkseth KE, Melhorn SJ, Schwartz MW, Schur EA. Longer T(2) relaxation time is a marker of hypothalamic gliosis in mice with diet-induced obesity. *Am J Physiol Endocrinol Metab.* 2013;304(11):E1245-E1250. doi:10.1152/ajpendo.00020.2013

61. Schroeter M, Franke C, Stoll G, Hoehn M. Dynamic changes of magnetic resonance imaging abnormalities in relation to inflammation and glial responses after photothrombotic cerebral infarction in the rat brain. *Acta Neuropathol.* 2001;101(2):114-122. doi:10.1007/s004010000262

62. Kigerl KA, Lai W, Rivest S, Hart RP, Satoskar AR, Popovich PG. Toll-like receptor (TLR)-2 and TLR-4 regulate inflammation, gliosis, and myelin sparing after spinal cord injury. *J Neurochem.* 2007;102(1):37-50. doi:10.1111/j.1471-4159.2007.04524.x

63. Goyal M, Sinha S, Ravishankar S, Shivshankar J. Case report: Reversible restricted diffusion and cytotoxic edema in the perilesional zone following continuous partial seizures. *Indian J Radiol Imaging.* 2008;18(03):227-229. doi:10.4103/0971-3026.41833

64. Koch S, Rabinstein A, Falcone S, Forteza A. Diffusion-weighted imaging shows cytotoxic and vasogenic edema in eclampsia. *Am J Neuroradiol.* 2001; 22(6):1068-1070.

65. Rosenblum WI. Cytotoxic edema: monitoring its magnitude and contribution to brain swelling. *J Neuropathol Exp Neurol.* 2007;66(9):771-778. doi:10.1097/nen.0b013e3181461965

66. Shepherd TM, Thelwall PE, Stanisz GJ, Blackband SJ. Aldehyde fixative solutions alter the water relaxation and diffusion properties of nervous tissue. *Magn Reson Med.* 2009;62(1):26-34. doi:10.1002/mrm.21977

67. Vergeldt FJ, Prusova A, Fereidouni F, et al. Multi-component quantitative magnetic resonance imaging by phasor representation. *Sci Rep.* 2017;7(1): 861. doi:10.1038/s41598-017-00864-8

68. Clark CA, Le Bihan D. Water diffusion compartmentation and anisotropy at high b values in the human brain. *Magn Reson Med.* 2000;44(6):852-859. doi:10.1002/1522-2594(200012)44:63.0.Co;2-a

69. Mulkern RV, Gudbjartsson H, Westin CF, et al. Multi-component apparent diffusion coefficients in human brain. *NMR Biomed.* 1999;12(1):51-62. doi:10.1002/(sici)1099-1492(199902)12:13.0.Co;2-e

70. Sehy JV, Ackerman JJ, Neil JJ. Evidence that both fast and slow water ADC components arise from intracellular space. *Magn Reson Med.* 2002;48(5): 765-770. doi:10.1002/mrm.10301

71. Echchannaoui H, Frei K, Schnell C, Leib SL, Zimmerli W, Landmann R. Toll-like receptor 2-deficient mice are highly susceptible to Streptococcus pneumoniae meningitis because of reduced bacterial clearing and enhanced inflammation. *J Infect Dis.* 2002;186(6):798-806. doi:10.1086/342845

72. Winters L, Winters T, Gorup D, et al. Expression analysis of genes involved in TLR2-related signaling pathway: Inflammation and apoptosis after ischemic brain injury. *Neuroscience.* 2013;238:87-96. doi:10.1016/j.neuroscience.2013.02.001

73. Pyatigorskaya N, Le Bihan D, Reynaud O, Ciobanu L. Relationship between the diffusion time and the diffusion MRI signal observed at 17.2 Tesla in the healthy rat brain cortex. *Magn Reson Med.* 2014;72(2):492-500. doi:10.1002/mrm.24921

74. Steven AJ, Zhuo J, Melhem ER. Diffusion kurtosis imaging: an emerging technique for evaluating the microstructural environment of the brain. *Am J Roentgenol.* 2014;202(1):W26-W33. doi:10.2214/AJR.13.11365

75. Jensen JH, Helpern JA, Ramani A, Lu H, Kaczynski K. Diffusional kurtosis imaging: the quantification of non-Gaussian water diffusion by means of magnetic resonance imaging. *Magn Reson Med.* 2005;53(6):1432-1440. doi:10.1002/mrm.20508

76. Lee JK, Liu D, Jiang D, et al. Fractional anisotropy from diffusion tensor imaging correlates with acute astrocyte and myelin swelling in neonatal swine models of excitotoxic and hypoxic-ischemic brain injury. *J Comp Neurol.* 2021;529(10):2750-2770. doi:10.1002/cne.25121

77. Jensen JH, Falangola MF, Hu C, et al. Preliminary observations of increased diffusional kurtosis in human brain following recent cerebral infarction. *NMR Biomed.* 2011;24(5):452-457. doi:10.1002/nbm.1610

78. Song SK, Sun SW, Ramsbottom MJ, Chang C, Russell J, Cross AH. Dysmyelination revealed through MRI as increased radial (but unchanged axial) diffusion of water. *NeuroImage.* 2002;17(3):1429-1436. doi:10.1006/nimg.2002.1267

79. Andersen KW, Lasič S, Lundell H, et al. Disentangling white-matter damage from physiological fibre orientation dispersion in multiple sclerosis. *Brain Commun.* 2020;2, fcaa077(2):fcaa077. doi:10.1093/braincomms/fcaa077

80. Guglielmetti C, Veraart J, Roelant E, et al. Diffusion kurtosis imaging probes cortical alterations and white matter pathology following cuprizone induced demyelination and spontaneous remyelination. *NeuroImage.* 2016;125:363-377. doi:10.1016/j.neuroimage.2015.10.052

81. Budde MD, Janes L, Gold E, Turtzo LC, Frank JA. The contribution of gliosis to diffusion tensor anisotropy and tractography following traumatic brain injury: validation in the rat using Fourier analysis of stained tissue sections. *Brain.* 2011;134(8):2248-2260. doi:10.1093/brain/awr161

82. Zhuo J, Xu S, Proctor JL, et al. Diffusion kurtosis as an in vivo imaging marker for reactive astrogliosis in traumatic brain injury. *NeuroImage.* 2012;59(1):467-477. doi:10.1016/j.neuroimage.2011.07.050

83. Song S-K, Sun SW, Ju WK, Lin SJ, Cross AH, Neufeld AH. Diffusion tensor imaging detects and differentiates axon and myelin degeneration in mouse optic nerve after retinal ischemia. *NeuroImage.* 2003;20(3):1714-1722. doi:10.1016/j.neuroimage.2003.07.005

84. Sun SW, Liang HF, Le TQ, Armstrong RC, Cross AH, Song SK. Differential sensitivity of in vivo and ex vivo diffusion tensor imaging to evolving optic nerve injury in mice with retinal ischemia. *NeuroImage.* 2006;32(3):1195-1204. doi:10.1016/j.neuroimage.2006.04.212

85. Sahin S, Çam I, Öztürk O, Efendi H, Anık Y, Gundogdu O. White matter evaluation in multiple sclerosis through magnetic resonance kurtosis imaging. *Cureus.* 2019;11(12):e6424. doi:10.7759/cureus.6424

86. Han Y, Wu P, Tian J, Chen H, Yang C. Diffusion kurtosis imaging and diffusion weighted imaging comparison in diagnosis of early hypoxic-ischemic brain edema. *Eur J Med Res.* 2023;28(1):159. doi:10.1186/s40001-023-01090-x

87. Veraart J, Poot DHJ, van Hecke W, et al. More accurate estimation of diffusion tensor parameters using diffusion Kurtosis imaging. *Magn Reson Med.* 2011;65(1):138-145. doi:10.1002/mrm.22603

88. Vanhoutte G, Pereson S, Delgado y Palacios R, et al. Diffusion kurtosis imaging to detect amyloidosis in an APP/PS1 mouse model for Alzheimer's disease. *Magn Reson Med.* 2013;69(4):1115-1121. doi:10.1002/mrm.24680

89. Praet J, Manyakov NV, Muchene L, et al. Diffusion kurtosis imaging allows the early detection and longitudinal follow-up of amyloid-beta-induced pathology. *Alzheimers Res Ther.* 2018;10(1):1. doi:10.1186/s13195-017-0329-8

90. Richard KL, Filali M, Prefontaine P, Rivest S. Toll-like receptor 2 acts as a natural innate immune receptor to clear amyloid beta 1-42 and delay the cognitive decline in a mouse model of Alzheimer's disease. *J Neurosci.* 2008;28(22):5784-5793. doi:10.1523/JNEUROSCI.1146-08.2008

91. Ullén F, Deliagina TG, Orlovsky GN, Grillner S. Visual pathways for postural control and negative phototaxis in lamprey. *J Neurophysiol.* 1997;78(2):960-976. doi:10.1152/jn.1997.78.2.960

92. Yanez J, Souto Y, Pineiro L, Folgueira M, Anadon R. Gustatory and general visceral centers and their connections in the brain of adult zebrafish: a carbocyanine dye tract-tracing study. *J Comp Neurol.* 2017;525(2):333-362. doi:10.1002/cne.24068

93. DeKorver NW, Chaudoin TR, Bonasera SJ. Toll-like receptor 2 is a regulator of circadian active and inactive state consolidation in C57BL/6 mice. *Front Aging Neurosci.* 2017;9:219. doi:10.3389/fnagi.2017.00219

94. Moore HA, Whitmore D. Circadian rhythmicity and light sensitivity of the zebrafish brain. *PLoS ONE.* 2014;9(1):e86176. doi:10.1371/journal.pone.0086176

SUPPORTING INFORMATION

Additional supporting information can be found online in the Supporting Information section at the end of this article.